

# Searching for Serendipitous Meteoroid Images in Sky Surveys

D. L. Clark • P. Wiegert

**Abstract** The Fireball Retrieval on Survey Telescopic Image (FROSTI) project seeks to locate meteoroids on pre-existing sky survey images. Fireball detection systems, such as the University of Western Ontario's ASGAR system, provide fireball state vector information used to determine a pre-contact trajectory. This trajectory is utilized to search databases of sky survey image descriptions to identify serendipitous observations of the impactor within the hours prior to atmospheric contact. Commonly used analytic methods for meteoroid orbit determination proved insufficient in modeling meteoroid approach, so a RADAU based gravitational integrator was developed. Code was also written to represent the description of an arbitrary survey image in a survey independent fashion, with survey specific plug-ins periodically updating a centralized image description catalogue. Pre-processing of image descriptions supports an innovative image search strategy that easily accounts for arbitrary object and observer position and motion.

**Keywords** meteor • meteoroid • pre-detection • sky survey • frustum • image search

## 1 Introduction

The association of in-space and in-atmosphere images provides a unique opportunity to correlate results from differing observation and modelling techniques. In-space and in-atmosphere observations both directly and indirectly yield conclusions as to object size, composition and dynamics. With the two observations of the same object, one is able confirm consistency, or highlight discrepancies, in existing methods. One would hope as well that the discovery of a pre-fireball meteoroid (PFM) would add to the understanding of the visual properties of Earth-impacting objects. The discovery of a PFM in space would serve to confirm or suggest refinements to methods used to calculate heliocentric orbits from fireball observations.

When work began on the FROSTI project in the summer of 2007, there had not been a single fireball object which had both been recorded in space on its approach to Earth, and recorded in the atmosphere as a fireball. The goal of FROSTI is to discover such dual observations through a systematic search of historical sky survey images for objects detected in all-sky camera systems. The initial data image survey targeted was the Canada-France-Hawaii Telescope Legacy Survey (CFHTLS) image catalogue (CFHT, 2009). A lofty goal of FROSTI was to be the first to relate in-space and in-atmosphere observations of a common object. However, that accomplishment was met with the pre-contact discovery of object 2008 TC3 by the Catalina Sky Survey (Jenniskens, et al., 2009) prior to the object's atmospheric entry over Liberia, and its subsequent meteorite deposit. Regardless, the FROSTI project continues with the intent to systematically arrive at further like observations.

---

D. L. Clark (✉) • P. Wiegert

Department of Physics and Astronomy, The University of Western Ontario, London, Ontario, Canada. Phone: +1-519- 657-6825; E- mail: dclark56@uwo.ca

The software used in this project is a pre-existing astronomical simulation package (ClearSky) developed by the author. Figure 1 depicts the flow of processing involved in searching for serendipitous images of PFMs using this software. (1) The atmospheric contact position and velocity state of the object, with error bars, are made available to ClearSky. This may involve the simple keying of an individual event or the development of custom plug-ins for event collections. The contact state information required is contact longitude, latitude and elevation, apparent radiant right ascension and declination, and the contact velocity, all with error bars. The software handles a variety of coordinate systems and reference frames. (2) A probability cloud of positional probability members is sampled from the input data and error bars. Each of these members is gravitationally integrated back in time for 48 hours, resulting in an ephemeris over time for each member. An orbit at infinity is calculated at the end of the integration of each member. The entire cloud of probability members is used to report a statistical orbit at infinity estimate with error bars. This orbit may be used as verification against published orbit elements, typically arrived at by analytic methods. (3) In preparation for image searching, sky survey updates are periodically downloaded to maintain a local generic image description catalogue. (4) The image catalogue is searched for candidate images using the generated ephemerides, and a simulated image is created for each candidate. (5) Using the simulated image as a guide, the actual sky survey image is manually searched for the PFM.

## 2 Modelling PFM Visibility

### 2.1 Primitive Modelling

The initial goal of modelling PFM visibility was to determine whether these objects are in fact visible for any significant duration of time prior to contact. Frequency distributions were not initially considered. PFM characteristics affecting visibility are size, distance from Earth and the Sun, phase angle, and albedo. Wiegert et al. (2007), extending on Bowell et al. (1989), document a relationship of asteroid diameter  $D$  in kilometers to absolute magnitude  $H_k$  and albedo  $A_k$  for colour filter  $k$  as:

$$D = \frac{1347 \times 10^{-H_k/5}}{A_k^{1/2}} \quad (1)$$

Disregarding colour filters, rearranging and combining with (7) and (8), and assuming a constant approach speed  $v$  such  $\Delta = vt$  that for a time  $t$  prior to contact, we derive a formula for apparent magnitude  $m$ : follows:

$$m = -5 \log_{10} \left( \frac{DA^{1/2}}{1347} \right) + 5 \log_{10}(rvt) - 2.5 \log_{10}((1 - G)\phi_1 + G\phi_2) \quad (2)$$

where:

$$\phi_1 = e^{-3.33(\tan(\frac{\alpha}{2}))^{0.63}}, \quad \phi_2 = e^{-1.87(\tan(\frac{\alpha}{2}))^{1.22}}$$

We now have an expression for apparent magnitude in terms of object diameter ( $D$ ) in metres, albedo ( $A$ ), velocity ( $v$ ) expressed consistently in units such that  $vt$  is in AU, phase angle ( $\alpha$ ) and time ( $t$ ), as well as solar distance ( $r$ ) and slope parameter ( $G$ ). Assuming  $r \sim 1$  AU in the proximity of Earth, and  $G = .15$  typical for low albedo asteroids, we are able to plot  $m$  against a sampling of reasonable  $D, A, v$  at  $a$  values, for various time periods.

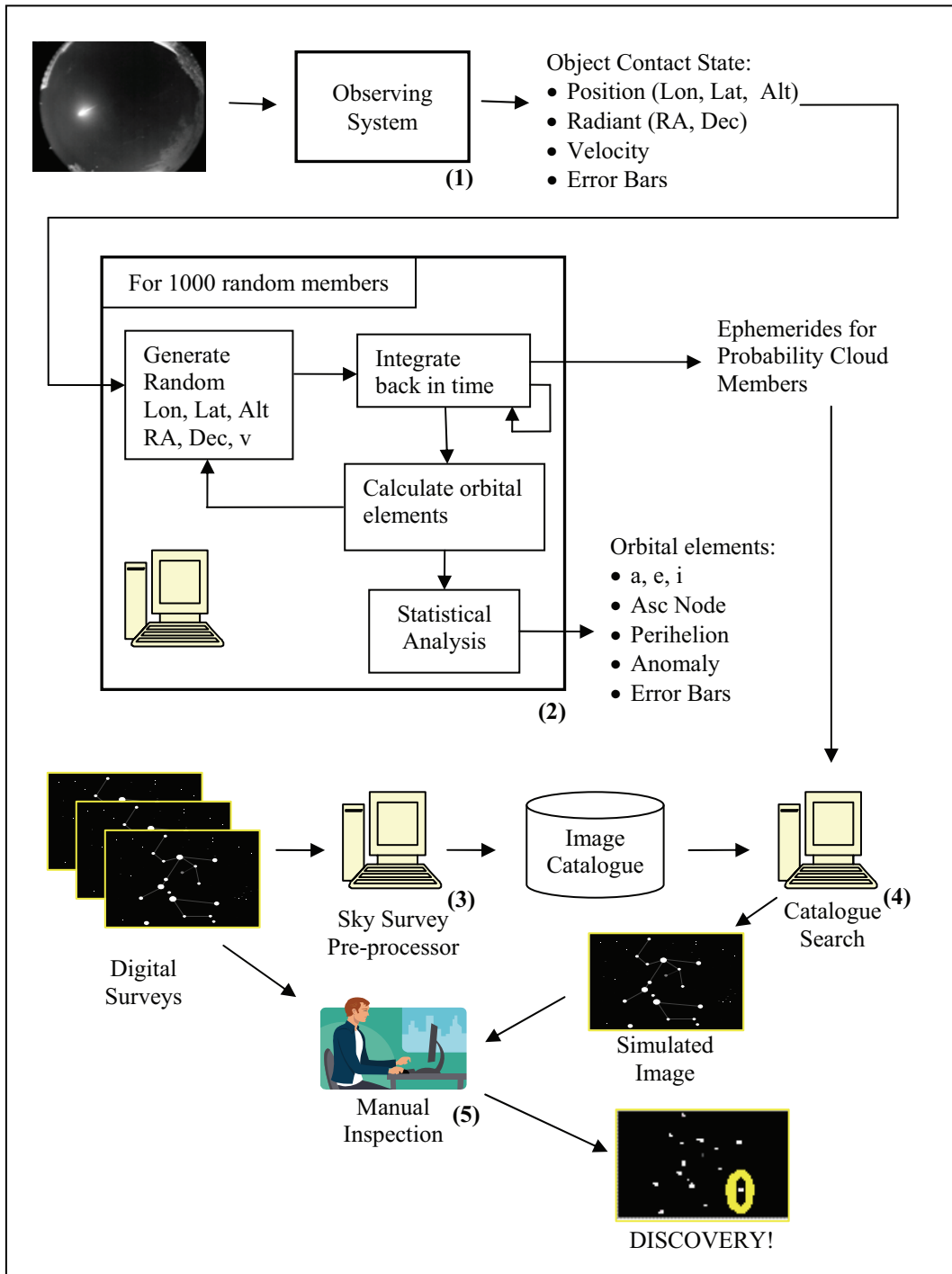


**Figure 1.** The process flow for PFM image searching, showing: (1) the transcription or importing of event contact state information and error bars, (2) the selection of a PFM probability cloud members, and the gravitational back integration of each member, resulting in ephemerides for each member, and a determination of orbit-at-infinity orbital elements, (3) the preprocessing of sky survey image descriptions into a generic image catalogue, (4) the searching for images based on PFM ephemerides, and (5) the manual inspection of candidate images for the PFM.

In Figure 2 visual magnitudes are plotted for objects with  $A = 0.05$  and  $0.25$ ,  $D = .25$  and  $1.0$  metres,  $v = 20, 30, 50$  and  $70 \text{ kms}^{-1}$ , and  $\alpha = 0^\circ, 30^\circ, 60^\circ, 90^\circ$  and  $120^\circ$  at 3 hour intervals from 3 hours to 48 hours prior to contact. Symbols in the plot represent each time interval, with lines connecting points of like interval. The CFHTLS visibility limit of 24th magnitude is shown for comparison. One observes in the plot that there are indeed combinations of PFM physical and dynamical attributes which support predetections. In addition to the expected favouring of higher albedo, larger diameter, slower speed, and lower phase angle objects, this plot demonstrates that very few objects remain visible for time periods in the range of the original project target of 48 hours, and that visibility ranges of 6-12 hours are more representative.

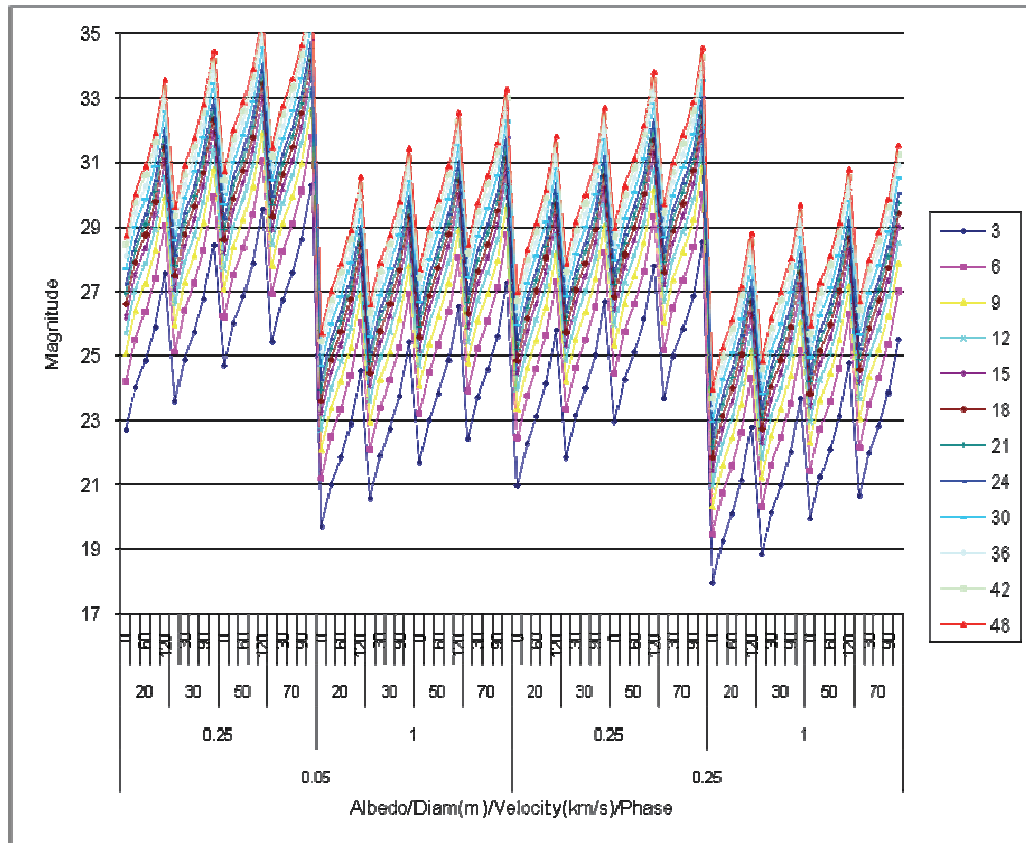


**Figure 2.** Plot of apparent magnitude over time of a variety of objects having albedo of 0.05 and 0.25, diameter of .25 and 1.0 metres, approach velocity of 20, 30, 50 and 70 kms-1, and phase angle 0°, 30°, 60°, 90° and 120°, assuming linear approach. The gray shaded area represents visibility within the CFHTLS images. Lines join points of equal visibility duration.

## 2.2 Bottke/Brown/Morbidelli Modelling

The simplistic modelling above, although reassuring that object prediction images could exist, does not provide insight into the frequencies of objects with attributes permitting successful predetections. For this we turn Near Earth Asteroid (NEA) dynamical models of Bottke et al. (2002a), fireball size frequency distribution and flux model of Brown et al. (2002), and the albedo model of Morbidelli et al. (2002a).

The Bottke 2002a NEA distribution is a 5-intermediate source model of NEA distribution binned over orbit semi-major axis ( $a$ ), eccentricity ( $e$ ), and inclination ( $i$ ). In addition to  $a$ ,  $e$ , and  $i$ , values for longitude of the ascending node ( $\Omega$ ), the argument of perihelion ( $\omega$ ) and true anomaly ( $f$ ) are required. In the case of the general NEA population, the three angles  $\Omega$ ,  $\omega$ , and  $f$  may be uniformly selected from the full 0-360° range, as there is no natural anti-symmetric bias to these elements. However, PFMs are characterized within the NEA population as objects which have the immediate potential to collide with the Earth. A standard equation for Keplerian motion is:

$$r = \frac{a(1-e^2)}{1+e \cos f} \quad (3)$$

where  $r$  is the object-Sun distance. Re-arranging, we have:

$$f = \pm \cos^{-1} \frac{a(1-e^2)-r}{er} \quad (4)$$

Selecting a uniformly random time  $t$  in the time range of interest, we are able to determine  $r$  by assuming  $r$  very closely approximates the Earth-Sun distance. The Earth-Sun distance is readily available from published theories such as DE405 (NASA JPL planetary position ephemerides available as tables of Chebyshev coefficients and supporting code).

Since the argument of perihelion  $\omega$  is defined as an angle from the ecliptic, the circumstance of Earth-object collision occurs on the ecliptic, and  $f$  is defined as an angle from  $\omega$ , we are able to determine  $\omega$  from  $f$ . There are four possible relationships among  $f$ ,  $\omega$ , and  $\Omega$  characterized by the object being at the ascending node or descending node, and whether the object is inbound or outbound in its orbit in relation to the Sun. These four cases are selected uniformly:

- 1) Ascending node, outbound:  $f = \cos^{-1} \dots, \omega = -f, \Omega = L$
- 2) Ascending node, inbound:  $f = -\cos^{-1} \dots, \omega = -f, \Omega = L$
- 3) Descending node, outbound:  $f = \cos^{-1} \dots, \omega = \pi - f, \Omega = \pi + L$
- 4) Descending node, inbound:  $f = -\cos^{-1} \dots, \omega = \pi - f, \Omega = \pi + L$

With approach characteristics handled, we must now model the size and albedo distributions which will impact visibility. Brown et al. (2002) describe a power law for the cumulative number of objects ( $N$ ) colliding with Earth per year with diameter  $\geq D$  in metres as:

$$\log N = c_0 - d_0 \log D \quad (5)$$

where  $c_0 = 1.568 \pm 0.03$  and  $d_0 = 2.70 \pm 0.08$ . Assuming a diameter of at least .2 m is required for visibility in telescopic images, equation (5) yields a flux of 2800 objects/year. This is not a large sample size at all when we consider that the samples are distributed over more than 15,000  $a$ ,  $e$ ,  $i$  bins in the Bottke distribution, and we still require a distribution over an albedo range. Therefore, the significantly larger sample is used, and resulting frequencies must be scaled back accordingly.

For albedo modelling we turn to Morbidelli et al. (2002a) who define 5 NEO albedo classes: Hig(h), Mod(erate), Int(ermediate), Low, and Com(etary) with a mean albedo for each, and albedo ranges for all but the Com class (for which we will assume the mean value for all samples). They then assign differing slope parameter values for each class to simulate a phase angle affect. Finally, they model a frequency distribution by class for the NEO population.

A sample of 10,000,000 objects was generated using the above NEA, bolide size and albedo models. This sample size is a compromise of reasonable required computation time against granularity

of result binning. For the strict needs of visual magnitude analysis, a smaller sample size could be used. However, other analyses (below) were performed on the model which benefited from the increased sample size. Figure 3 shows the visual magnitude distribution of the sample objects plotted over various times from 5 minutes to 24 hours prior to Earth contact. As in the simple model of above, a significant portion of objects are potentially visible (magnitude <24) in sky surveys in the minutes prior to contact. However, this visible proportion trails off very quickly in the hours prior to contact, to the extent that almost none of the model population have visual magnitude less than 6 hours prior.

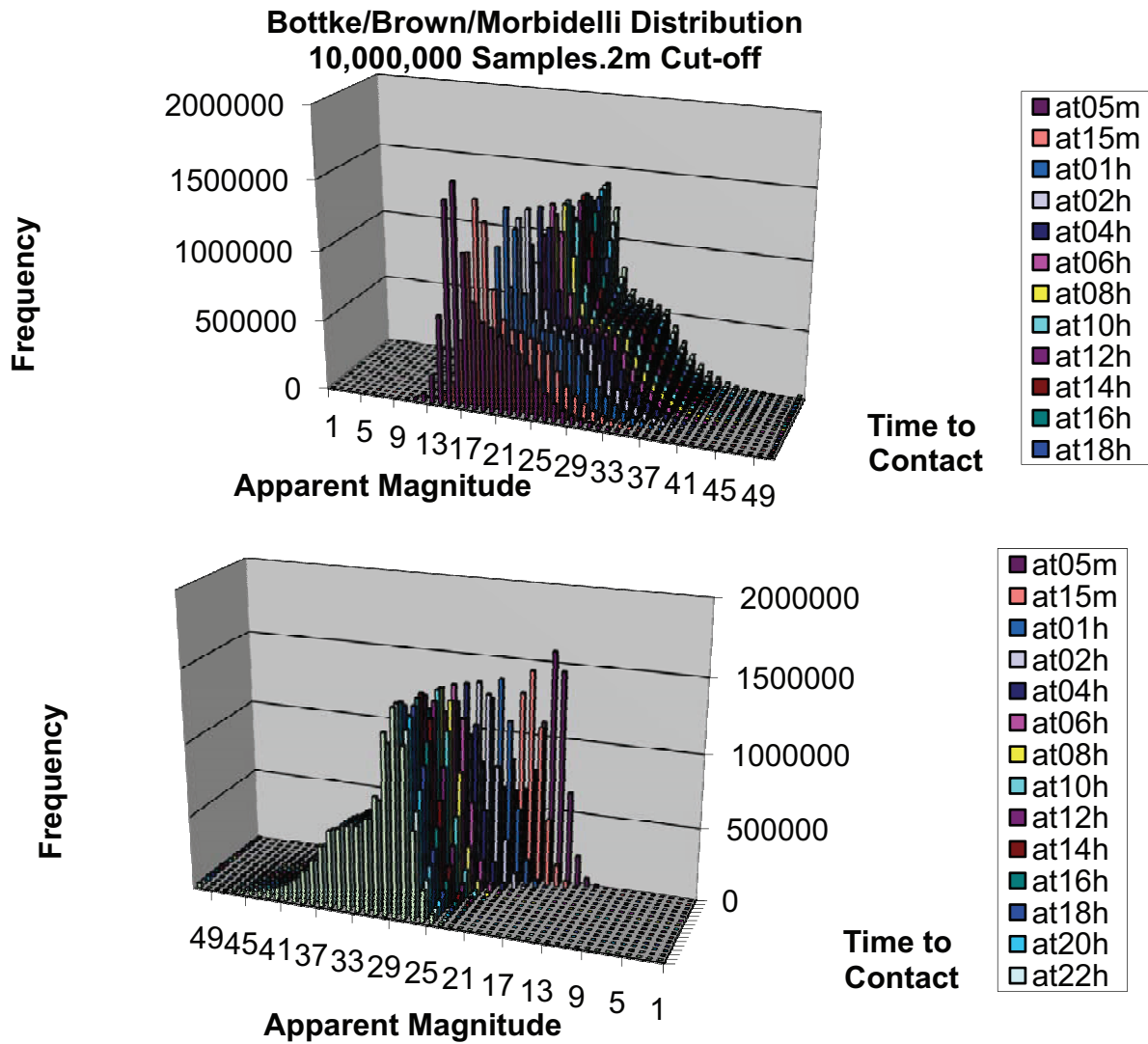


**Figure 3.** A visual magnitude plot of 10,000,000 simulated objects generated from the Bottke et al. (2002a) NEA distribution, the Brown et al. (2002) bolide size-frequency distribution, and the Morbidelli et al. (2002a) albedo distribution. Only objects above .2m in diameter are considered. Objects are selected by adjusting the argument of perihelion such that objects collide with Earth. The plot shows the number of objects falling into 1-magnitude wide bins over a series of time intervals prior to contact. Top: From foreground to background are the time intervals of 5 minutes, 15 minutes, 1 hour, and 2 hours to 24 hours in 2-hour increments. Bottom: The same plot with earlier times in the foreground.

### 3 Determination of PFM Trajectory

The search for a nearby object in sky surveys requires an accurate ephemeris for the object, with a good understanding of the errors in position over time. It is insufficient to use the published orbital elements of a PFM, elements that are typically derived using analytical means. The elements are expressed in far too little accuracy to be useful; for example a semi-major axis expressed to the precision of .001 AU yields errors rivalling the radius of the orbit of the Moon. As well, published orbits are orbits at infinity, not reflecting the impact of the Earth's gravity on the approach trajectory. Instead, an accurate translation of the PFM's contact state into heliocentric coordinates and a full gravitational integration are required.

#### 3.1 Calculating the PFM Heliocentric Contact State

The heliocentric contact state of an object is represented as a cloud of probability members, each member having longitude  $\lambda_B$ , latitude  $\varphi_B$ , height  $h_B$ , radiant right ascension and declination  $\alpha_R$  and  $\delta_R$ , and velocity  $v_\infty$ , all at an epoch  $t$ , where each of these values, including the epoch, are generated from a Gaussian distribution defined by the reported mean and standard deviations. Each member's contact state is converted to heliocentric coordinates, in preparation for the integration of each member, as follows:

- 1) The geocentric coordinates centred on Greenwich ( $x_G, y_G, z_G$ ) are calculated using the WGS84 theory.
- 2) The mean rotation of the Earth  $\theta$  is calculated using the methods of Meeus (1991) Chapter 11.
- 3) The apparent sidereal rotation of the Earth  $\theta'$  is calculated from  $\theta$  as described in Chapters 11 and 21 of Meeus (1991). This involves the calculation of the mean obliquity of the ecliptic  $\epsilon_0$ , the nutation in longitude  $\Delta\Psi$ , and the nutation in obliquity  $\Delta\epsilon$ . The calculations of nutation and obliquity require that the time of the event be expressed in Dynamical Time ( $TD$ ), not universal time (UT). This difference in these timeframes is taken from a table of adjustments available on the US Naval Observatory web site (USNO, 2010).
- 4) We are then able to rotate ( $x_G, y_G, z_G$ ) by  $\theta'$  giving the Earth-centred equatorial coordinates with respect to the equinox of the date ( $x_E, y_E, z_E$ ).
- 5) ( $x_E, y_E, z_E$ ) are converted to the equinox J2000 ( $x_{EJ}, y_{EJ}, z_{EJ}$ ) by converting to spherical coordinates, precessed to J2000 by the methods of Meeus (1991) Chapter 20, and converting back to rectangular coordinates. We retain the right J2000 right ascension  $\alpha_E$  for later use.
- 6) The apparent contact velocity of the PFM equinox J2000 ( $v_{x0J}, v_{y0J}, v_{z0J}$ ) is calculated directly from  $\alpha_R, \delta_R$ , and  $-v_\infty$ .
- 7) The velocity due to the rotation of the Earth ( $v_{xRot}, v_{yRot}, v_{zRot}$ ) is the tangent vector at the Earth-centred position expressed in equatorial coordinates for the epoch of the date. The magnitude  $v_{ROT}$  of the velocity is taken from a complete rotation of the earth at the object's distance and declination. Care must be taken when velocities are tracked in software with respect to solar time scales; we must make a sidereal adjustment. ( $v_{xRot}, v_{yRot}, v_{zRot}$ ) is then calculated from  $v_{ROT}$  and  $\alpha_E, v_{zRot}$  being 0.
- 8) ( $v_{xRot}, v_{yRot}, v_{zRot}$ ) are converted to equinox J2000 ( $v_{xRotJ}, v_{yRotJ}, v_{zRotJ}$ ) as in 5) above.
- 9) We arrive at an Earth-centred equatorial J2000 velocity ( $v_{xEJ}, v_{yEJ}, v_{zEJ}$ ) by summing ( $v_{x0J}, v_{y0J}, v_{z0J}$ ) and ( $v_{xRotJ}, v_{yRotJ}, v_{zRotJ}$ ).

- 10) The Earth-centred equatorial J2000 position  $(x_{EJ}, y_{EJ}, z_{EJ})$  and velocity  $(v_{xEJ}, v_{yEJ}, v_{zEJ})$  are converted to heliocentric coordinates  $(x_{EH}, y_{EH}, z_{EH})$  and  $(v_{xEH}, v_{yEH}, v_{zEH})$  by adding the Earth's position at the epoch using the JPL Horizons DE405 ephemeris. The epoch must be expressed in Terrestrial Time ( $TT$ ), equivalent to  $TD$  as calculated in 3).
- 11) These equatorial coordinates are converted to heliocentric ecliptical coordinates  $(x_H, y_H, z_H)$  and  $(v_{xH}, v_{yH}, v_{zH})$  by converting to spherical coordinates, converting to ecliptical coordinates as in Meeus (1991) Chapter 12, and converting back to rectangular coordinates. These calculations again require  $\varepsilon_0$  and  $\Delta\varepsilon$  as calculated in 3).

### 3.2 Integrating the PFM Trajectory

Not wanting to re-invent the wheel in the field of numerical integrators, and understanding that this application did not require sophisticated optimizations or approaches in performance, we decided on a quick rework of an existing C-language implementation of RADAU-15, a 15th-order differential equation integrator documented in Everhart (1985). The RADAU family of integrators is characterized by the use of Gauss-Radau spacings for sequence sub-steps. The work of porting and integrating the publically available C-code involved converting C code to C++, the language used in the remainder of the project coding, and abstracting the concepts of an integrator, force calculations, and physical objects into C++ interfaces and implementations to facilitate substitution of trial implementations. The initial implementation of the RADAU integrator was tested by integrating the major objects of the solar system over 100 years, and comparing the results to the JPL DE405/DE406 ephemerides. A full integrator-to-DE405/406 comparison was performed, with acceptable results (for example: .6" error in solar longitude for Mars, with an oscillating .000003 AU error in solar distance after 100 years). This test required the implementation of post-Newtonian adjustments, a refinement not required for the integration of meteoroid objects on Earth-approach. These post-Newtonian adjustments require knowledge of velocity state within the inter-object force calculations that is not required by PFM integrations.

The resulting integration back in time of a collection of probability points generated from contact state value and error bars yields a slowly expanding probability cloud representing the possible meteoroid paths. Figure 4 is a sample illustration of the Bunburra Rockhole event, generated from an initial contact state provided by Pavel Spurný in a private correspondence (Spurný, 2009). The convergence of the probability cloud towards the eventual error bars in the original state is evident.

### 3.3 Comparison to Ceplecha Analytical Orbits

The analytical orbit-at-infinity calculation methods of Ceplecha (1987) provide the means to verify the resulting orbits from the back-integration technique. Two sets of fireball orbits derived using Ceplecha's calculations were used to perform this comparison: the ten largest mass European Network events from 1993-1996 documented in Spurný (1997), and 10 more recent unpublished European Network events provided by Spurný in a private correspondence (Spurný, 2010). For the purposes of orbit-at-infinity calculations, the back-integrations are stopped at 2-months prior to Earth contact. Figure 5 demonstrates the good correspondence between the methods for the Spurný (1997) events. Results on the later events await Spurný's publication of his results.

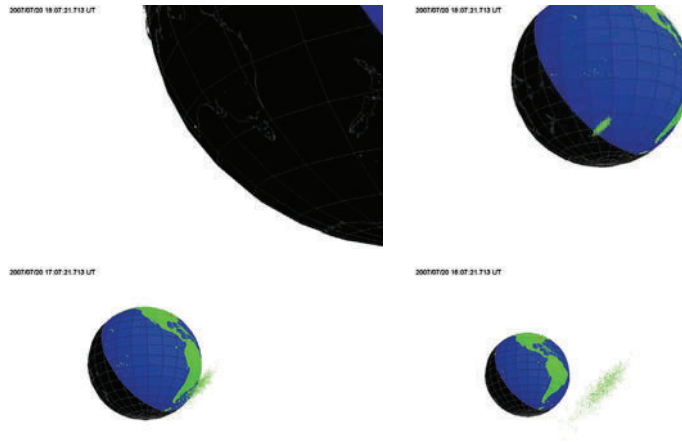


**Figure 4.** The RADAU-15 generated probability cloud for the Bunburra Rockhole effect. Meteoroid contact position, velocity and error bars were provide by Pavel Spurný in private correspondence (Spurný, 2009). The illustrations show the probability at the time of contact, and 1, 2 and 3 hours prior to contact. The viewer is a consistent 9100 km distance from the cloud's mean point.

Event	Source	a	a SD	e	e SD	i	i SD	node	node SD	peri	peri SD
EN070594(Leszno)	ClearSky	2.1070	0.0172	0.5328	0.0037	6.8953	0.0838	227.1320	0.0004	338.2490	0.2630
	Published	2.1000	0.0200	0.5320	0.0040	6.9100	0.0700	227.1100	0.0001	338.2000	0.2000
	Delta	0.0070	-0.0028	0.0008	-0.0003	-0.0147	0.0138	0.0220	0.0003	0.0490	0.0630
EN070893(Polná)	ClearSky	2.0040	0.0283	0.5163	0.0070	18.8955	0.2539	135.4610	0.0004	209.5240	0.0727
	Published	2.0030	0.0060	0.5162	0.0013	18.9000	0.0300	135.4410	0.0002	209.5200	0.0700
	Delta	0.0010	0.0223	0.0001	0.0057	-0.0045	0.2239	0.0200	0.0002	0.0040	0.0027
EN150294(Dresden)	ClearSky	2.3386	0.0132	0.5784	0.0023	33.8443	0.0347	327.1350	0.0000	173.9130	0.1768
	Published	2.3380	0.0030	0.5783	0.0006	33.8410	0.0120	327.1300	0.0001	173.9000	0.0200
	Delta	0.0006	0.0102	0.0001	0.0017	0.0033	0.0227	0.0050	-0.0001	0.0130	0.1568
EN150396(Dobříš II)	ClearSky	7.5345	1.4256	0.8779	0.0204	8.3313	0.4868	355.5680	0.0007	141.1660	0.9380
	Published	7.2000	1.1000	0.8800	0.0200	8.3000	0.5000	355.5530	0.0001	141.2000	0.9000
	Delta	0.3344	0.3256	-0.0021	0.0004	0.0313	-0.0132	0.0150	0.0006	-0.0340	0.0380
EN220293(Meuse)	ClearSky	1.5069	0.0181	0.5682	0.0036	32.5929	0.1559	334.4100	0.0000	266.8560	0.8100
	Published	1.5000	0.0200	0.5670	0.0040	32.6000	0.2000	334.4070	0.0001	266.9000	0.8000
	Delta	0.0069	-0.0019	0.0012	-0.0004	-0.0071	-0.0441	0.0030	-0.0001	-0.0440	0.0100
EN220495A(Koutim)	ClearSky	2.3878	0.0105	0.7886	0.0008	4.1310	0.0462	32.4134	0.0002	277.3980	0.0788
	Published	2.3740	0.0040	0.7878	0.0003	4.1190	0.0120	32.3858	0.0001	277.5800	0.0500
	Delta	0.0138	0.0065	0.0008	0.0005	0.0120	0.0342	0.0276	0.0001	-0.1820	0.0288
EN231195(J. Hradec)	ClearSky	3.4436	0.1283	0.7813	0.0070	11.8921	0.5959	240.3480	0.0002	242.7970	1.9673
	Published	3.3900	0.0500	0.7790	0.0030	11.9900	0.0200	240.3360	0.0007	243.3000	0.3000
	Delta	0.0536	0.0783	0.0023	0.0040	-0.0979	0.5759	0.0120	-0.0005	-0.5030	1.6673
EN241095B(Odra)	ClearSky	1.3055	0.0859	0.5663	0.0193	52.7598	0.5480	211.0410	0.0006	281.4500	4.2692
	Published	1.3270	0.0110	0.5710	0.0020	52.8000	0.2000	211.0380	0.0007	280.2000	0.4000
	Delta	-0.0216	0.0749	-0.0047	0.0173	-0.0402	0.3480	0.0030	-0.0001	1.2500	3.8692
EN250594(Ulm)	ClearSky	2.0128	0.1134	0.5548	0.0214	2.5661	0.7510	244.4780	0.0293	312.0790	1.7704
	Published	2.0400	0.0200	0.5600	0.0030	2.5000	0.0400	244.5260	0.0007	313.1000	0.3000
	Delta	-0.0272	0.0934	-0.0052	0.0184	0.0661	0.7110	-0.0480	0.0286	-1.0210	1.4704
EN251095A(Tisza)	ClearSky	1.0780	0.0069	0.8068	0.0010	6.1339	0.1655	31.2538	0.0003	140.4080	0.3306
	Published	1.0770	0.0090	0.8067	0.0010	6.2000	0.2000	31.2595	0.0001	140.4000	0.4000
	Delta	0.0010	-0.0021	0.0001	0.0000	-0.0661	-0.0345	-0.0057	0.0002	0.0080	-0.0694

**Figure 5.** A list of the 10 highest mass events from Spurný (1997) showing the published orbital elements calculated using Ceplecha (1987) calculations compared to the orbit at infinity elements calculated using the project's software ClearSky's integration technique. Semimajor axis, eccentricity, inclination, longitude of the ascending node and argument of perihelion are listed. Standard deviations are listed beside each element. ClearSky elements are displayed in blue if outside the published error bars. Published elements are displayed in red if outside the ClearSky calculated error bars. Note that the ascending nodes are numerically close, but are consistently flagged as being out of the corresponding error bars.

The close correspondence of orbit elements from the Ceplecha and integration techniques serves as both a validation for the time-honoured analytical method, and as a confirmation the integration technique does accurately reproduce object approach trajectories. However, the small but systematic variance in longitude of ascending node garnered further attention. Section 11 of Ceplecha (1987) describes in detail the impact of Earth's gravity on calculating velocity and radiant direction of a meteor, this impact being removed prior to the calculation of orbital elements. However, in formula (48) of Section 11, Ceplecha makes the assumption that the longitude of the ascending node ( $\Omega$ ) of the orbit can be directly derived from the solar longitude of the Earth ( $L_{SUN}$ ) at the time of impact. This is true of the instantaneous orbit of the meteoroid, but not its orbit at infinity. The instantaneous  $\Omega$  is drawn towards the limiting value  $L_{SUN}$  as the meteoroid approaches the Earth. The magnitude of this shift in  $\Omega$  depends on the approach characteristics and the length of time the meteoroid is influenced by Earth's gravity. The largest calculated variance in  $\Omega$  is  $.15^\circ$  for Spurný (2010) event EN231006. Figure 6 demonstrates the shift in ascending node of approximately  $.1^\circ$  of the Bunburra Rockhole event. A consequence of this variance in  $\Omega$  that has not been quantified is the dependency in the Ceplecha calculations of all other orbit elements except semimajor axis on  $\Omega$  and  $L_{SUN}$ . Further quantification of the impact is noted as possible future work.

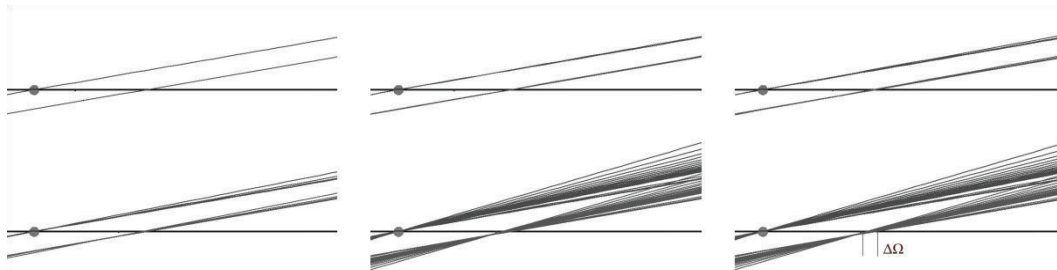


**Figure 6.** The shift  $\Delta\Omega$  of the ascending node  $\Omega$  of the instantaneous orbit of the Bunburra Rockhole meteoroid. From left to right, top to bottom, the progress of the shift is shown, 4, 3, 2, and 1 hours prior to contact, at contact, and at contact with the shift highlighted. The rightmost diagonal lines represent the instantaneous orbits at the ascending node on the near side of the Sun. The leftmost lines represent the orbits at the descending node on the far side of the Sun.

## 4 Searching Sky Surveys

### 4.1 Image Frustums

Astronomical images are typically thought of as two-dimensional rectangular projections onto the celestial sphere. Such images may be defined by the right ascension ( $\alpha$ ) and declination ( $\delta$ ) of the four corners of the image, or by the  $\alpha$  and  $\delta$  of the image centre, width and height of the image, and the rotation around the image centre. The computations involved in determining the location of a fast moving object in relation to a long image exposure involves several conversions of the object's position into observer centred  $\alpha$  and  $\delta$  as both the object and observer move over time. These conversions, although not complex, are computationally expensive as they involve trigonometric transformations. Since the position of an object is relative to the observer, there is little opportunity to optimize this heavy computation against multiple images, or against multiple image surveys. I therefore developed an image representation scheme which supports a front-end loaded one-time optimization of individual image representations, while reducing the object-image computation complexity.

A single survey image in reality is a projection of a three-dimensional volume of space. Assuming a rectangular image, this volume is a frustum as shown in Figure 7. A frustum is defined as the portion of a solid lying between two planes. An image frustum is the portion of a square pyramid lying between a front viewing plane and an arbitrary depth of field plane. This real-world frustum space can be transformed into a three dimensional rectangular 2x2x1 frustum space to which object position intersections are easily calculated. The determination of the image frustum and the calculation of the transformation into a rectangular frustum space are costly, but may be performed once per image description with the resulting transformation being stored and associated with the image description. Viewing frustums and the related transformations have been used for decades in rendering three dimensional world scenes onto a two-dimensional view port (screen). In particular, I have leveraged the unpublished lecture notes and course exercises by Beatty (1980).

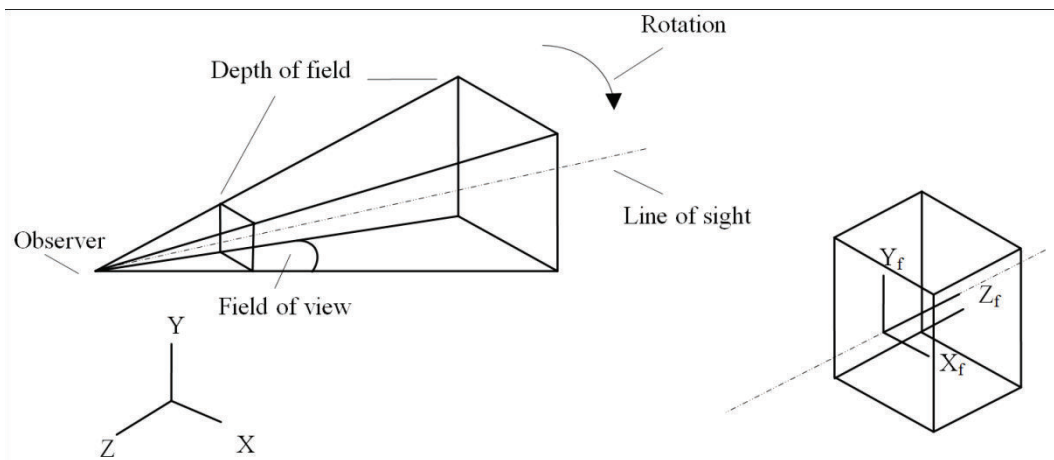


**Figure 7.** An image frustum in heliocentric space, and the rectangular frustum space. Any astronomical image is a representation of the three dimensional frustum volume defined by the observer location, the field and depth of view of the image, the line of sight, and the rotation of the image. Points in heliocentric space may be easily transformed into points in the frustum space, facilitating image-object intersection and object motion characterization.

An image frustum is defined by a set of parameters: observer position  $(d_x, d_y, d_z)$ , a line of sight  $(s_x, s_y, s_z)$ , horizontal and vertical fields of view  $(\alpha_h, \alpha_v)$ , a near view distance  $(d)$ , taken as a distance closer to the observer than the typical in-atmosphere meteor distance), and a depth of field  $(f)$ , taken as infinity). It can be shown that the real-world frustum space may be transformed into a rectangular frustum space based on a number of constituent transformations using the above frustum parameters. A PFM position (or the position of any solar system object) in heliocentric coordinates  $(x, y, z)$  may be translated to the image frustum space  $(x_f, y_f, z_f)$  by the simple application of a 4x4 transformation matrix  $T_f$  to the homogenous coordinates  $(x, y, z, 1)$ , where  $T_f$  is the matrix product of a series of constituent transformations:

$$[x, y, z, 1][T_F] = [x_f, y_f, z_f, w_f] \tag{6}$$

An object's position with respect to the 2x2 image frustum front face is:

$$x_I = \frac{x_f}{w_f}, y_I = \frac{y_f}{w_f} \quad (7)$$

where  $-1 \leq x_I \leq 1$  and  $-1 \leq y_I \leq 1$  correspond to the object being on the image. Additional outputs of the above transformation are four values called edge coordinates, which allow for quick object-image checking, prior to performing the above divisions in calculating  $x_I$  and  $y_I$ :

$$\begin{aligned} e_1 : w_f + x_f & : \text{left edge} \\ e_2 : w_f - x_f & : \text{right edge} \\ e_3 : w_f + y_f & : \text{bottom edge} \\ e_4 : w_f - y_f & : \text{top edge} \end{aligned}$$

In all cases, the edge coordinate  $e_i$  exhibits the properties:

$$\begin{aligned} e_i > 0 & \quad \text{the position is inside the edge} \\ e_i < 0 & \quad \text{the position is outside the edge} \end{aligned}$$

As long as the  $4 \times 4$   $T_f$  transformation matrix is calculated before search time, the computation required to determine an object-image intersection at a single point in time is the 12 multiplications and 9 additions required to calculate the  $x_f$ ,  $y_f$ , and  $w_f$  values, and the 4 additions and 4 comparisons required to perform the edge coordinate checks. The edge coordinates provide a means to quickly determine the characteristics of an object's motion on, off, or through the image by comparing beginning-of-exposure coordinates to end-of-exposure coordinates.

## 4.2 Automated Downloads and Pre-processing

The object-image intersection process described above assumes the opportunity to possess pre-calculated image frustum descriptions and transformations prior to executing object searches. I have developed a generic image catalogue data base which serves to: 1) maintain local copies of available image databases, 2) provide a generic representation of the images databases, 3) support the storage of the above pre-calculated data, and 4) provide indexing to support various object search use cases. The image catalogue developed for this project is implemented as a flat file of generic image data referring back to local copies of downloaded image databases. Indexes are maintained on the image catalogue to facilitate searching by survey name, time frame, or both. The image catalogue is recreated from scratch on every download cycle. This approach was taken to avoid the concerns of needing a sophisticated underlying database technology that could handle both efficient insertion and querying. The download of updates from each image survey can be implemented as either a periodic replacement of the survey data, or as a net-change update. If the downloaded survey catalogue is represented in an easily parsed fixed form, then the survey import may be implemented by simply defining the survey catalogue in meta-data. If the survey data is difficult to parse, a survey plug-in may be developed to implement the import. Figure 8 describes the contents of the generic image catalogue records.

## 4.3 General Use of the Image Search Algorithm

The image representation described above and the resulting search based on ephemerides is a generic method which is independent of the source of the image and the target being searched. The

Image Collection	The name of the image survey, database, or collection. E.g. “CFHT Catalogue”, “Catalina Catalogue”.
Image File	The local copy of each image survey is described by one or more file names, and a description of the format of these files. The image catalogue points to the file number and file offset corresponding to an image in this set of files.
Image Offset	The position in the image file where the source description of the image may be found (see Image File).
Right Ascension	The right ascension of the centre of the image.
Declination	The declination of the centre of the image.
Width	The width of the image in radians.
Height	The height of the image in radians.
Start Time	The start date and time of the image exposure.
Exposure	The length of the exposure in seconds.
Starting Frustum	The parameters used to describe the image frustum at the beginning of the exposure, and the contents of the 4x4 transformation matrix used to convert object positions to the frustum space. The frustum description includes: <ul style="list-style-type: none"> <li>• Frustum rotations around each axis</li> <li>• Dimensions of the frustum front face</li> <li>• Observer distances to the front and back faces</li> <li>• 16 numbers corresponding to the <math>T_f</math> image frustum transformation.</li> </ul>
Ending Frustum	The parameters used to describe the image frustum at the end of the exposure (See Starting Exposure)

**Figure 8.** Image catalogue record description.

technique is therefore easily adapted to any use where the image source and target object are in motion. Whereas the original need of this project was to provide a flexible system that would support a variety of telescopic sky surveys, the approach can be easily extended to cover other image sources, such as spacecraft image databases, and amateur astrophoto collections. In addition, support sky surveys may be searched for any solar system object. For example, in support of the article Gilbert and Wiegert (2009), ClearSky was used to search the CFHTLS for images of three main-belt comets: 133P/Elst-Pizarro, P/2005 U1 (Read), and 176P/LINEAR. Images of 176P/LINEAR were located, including a set of three images dated 2007 January 15. Figure 9 shows the image search result file for that period. Figure 10 shows the three image simulations, and the corresponding close inspection images created by Wiegert from CFHTLS image downloads.

## 5 Results to Date and Future Work

At the time of writing, this project has not yielded a discovery of a PFM image, however searching will continue. The results of the project have been of a more indirect nature, with our gaining understanding of PFM visibility and the nature of PFM orbits. The project has also contributed to the science with a confirmation of the heavily relied-upon analytical methods of the past 30 years, and by providing a useful general image catalogue search technique.

### 5.1 Image Searches

CFHTLS image searches have been performed on two collections of European Network events as documented in Spurný (1997) and Spurný (2010), as well as three individual events: Grimsby (McCausland, et al., 2010), Bunburra Rockhole (Bland, et al., 2009) and (Spurný, 2009), and Buzzard Coulee (Hildebrand, et al., 2009). No images have yet been found. The implementation of Spacewatch

	A	B	C	D	E	F	G	H	I	J
1	Collection:	CFHT Catalogue								
2	Image ID:	889493								
3	Object:	(118401) LINEAR								
4	Start Time:	2007/01/15 09:33:29 UT								
5	Start X pos:	-0.926								
6	Start Y pos:	-0.818								
7	StdDev in X:	0.000								
8	StdDev in Y:	0.000								
9	On-image Prob%:	100.0%								
10	EndTime:	2007/01/15 09:35:59 UT								
11	End X pos:	-0.925								
12	End Y pos:	-0.818								
13	StdDev in X:	0.000								
14	StdDev in Y:	0.000								
15	On-image Prob%:	100.0%								
16	Abs Magnitude:	15.1								
17	App Magnitude:	19.7								
18	Phase angle:	3.7°								
19	Pos Method:	Ephemeris								
20	@name:	889493								
21	@ra:	463953750								
22	@dec:	69058900								
23	object:	5A10								
24	category:	CAL								
25	filter:	R.MP9601								
26	obstype:	OBJECT								
27	crunid:	06BM06								
28	runid:	2006BF41								
29	@exp:	150.1100006								
30	@time:	Jan 15 2007 9:33:29:000AM								
31	public_date:	Feb 29 2008 10:00:00:000AM								
32	qso_status:									
33	is_phot:									
34	obs_iq_refccd:									
35	procddate:	Feb 17 2007 11:22:18:000AM								
36	elixirsvw:	2								
37	flipssvw:	3								
38	URL:	<a href="http://www.cadc.hia.nrc.gc.ca/authProxy/getData?archive=CFHT&amp;asf=true&amp;file_id=889493p">http://www.cadc.hia.nrc.gc.ca/authProxy/getData?archive=CFHT&amp;asf=true&amp;file_id=889493p</a>								

**Figure 9.** One image result from the CFHTLS catalogue search result file for 176P/LINEAR for the period of January 2007. Three images were located, the details of each circumstance represented in an Microsoft Excel spreadsheet tab. The result file text contains image description information (including the URL for downloading the CFHTLS image), object visibility, and the position of the object in the image. The X,Y coordinates of the object in the image (ranging from -1 to 1) are reversed due to the orientation of the image. The green arrow has been added to show the position of the object.

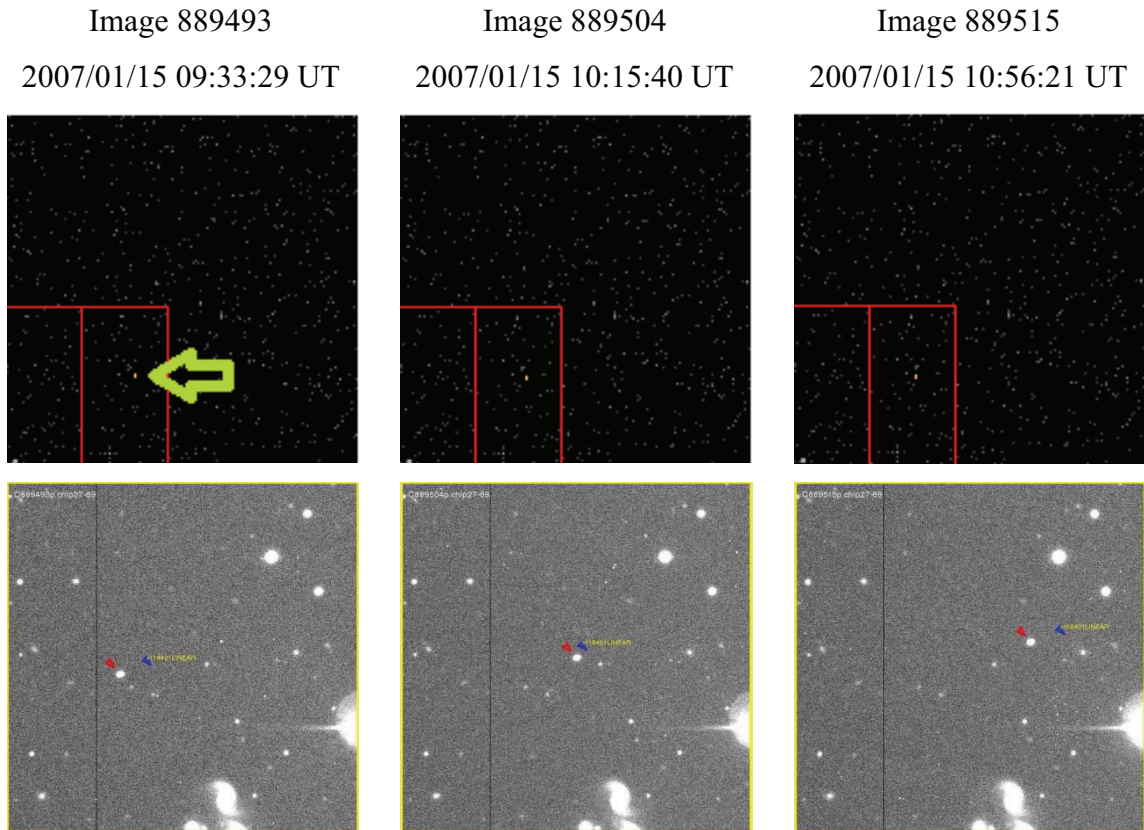


**Figure 10.** Top row: Detail from the three simulated CFHTLS images from 2007 January 15 showing object 176P/LINEAR. The green arrow has been added to highlight the object position. Note the slight movement in the object. Bottom row: Extractions from the actual CFHTLS images created by Dr. Paul Wiegert. The red arrow indicates the actual object; the blue arrow indicated the expected position based on the MPC orbit published at the time. Orientations between the simulations and the extractions are opposite.

(McMillan, 2010) and Catalina (Beshore, 2010) sky survey downloads are complete, and discussions are ongoing regarding access to the PanSTARRs (Jedicke, 2010) survey data. Contact state information on any additional significant fireball events is most welcome. As described above, the search techniques have shown useful in discovering serendipitous images of other solar system objects.

## 5.2 Modelling Results

As the project progressed, the realization developed that the chance of linking a fireball observation to a serendipitous PFM image is low. The modelling performed shows that a sufficiently large event in any one given meteor detection network is, at the optimistic end, a yearly event. Conservatively, in the case of ASGARD, it is a decadal event. Survey effectiveness analyses show that the chances for telescope detection can be severely reduced by object or solar geometry, as well as the quickly reducing apparent magnitude of the PFM. Finally, the chance of success is further reduced by the unmodelled but evidently small probability of a survey telescope being pointed at the correct field in relation to its overall sky coverage capability or preference. However the possibility of success remains enticing. Of particular note is the level of genuine interest shown for this project by the many people with whom I have discussed the work. Those involved in sky surveys seem eager to make their data available, and

those analysing various fireball events are eager to provide and transform their data for use in this project.

### 5.3 Orbit Determination Results

A major accomplishment of this project was the confirmation of the Ceplecha (1987) orbit determination methods, and the offering of an adjustment of that work to account for a shift in the PFM's longitude of the ascending node. In verbal conversations with Dr. Pavel Spurný and others, it has been stated that this validation of Ceplecha's methods has not been done before, even though they are widely used. There can now be an increased level of confidence in the orbits derived from those methods.

### Acknowledgements

I thank Dr. Paul Wiegert (UWO) for his support and technical assistance in this project, Dr. Peter Brown (UWO) and Dr. Pauline Barmy (UWO) for their support and advice, Rob Weryk (UWO) and Zbyszek Krzeminski (UWO) for their infinite patience in explaining the ASGARD system and for preparing data for my analysis, Dr. Pavel Spurný (Astronomical Institute, Academy of Sciences of the Czech Republic) for his explanations and data allowing me to compare methods to the Ceplecha work, and my wife Angela for her proof-reading.

This work is based in part on observations obtained with MegaPrime / MegaCam, a joint project of CFHT and CEA/DAPNIA, at the Canada-France-Hawaii Telescope (CFHT) which is operated by the National Research Council (NRC) of Canada, the Institut National des Science de l'Univers of the Centre National de la Recherche Scientifique (CNRS) of France, and the University of Hawaii. This work is based in part on data products produced at TERAPIX and the Canadian Astronomy Data Centre as part of the Canada-France-Hawaii Telescope Legacy Survey, a collaborative project of NRC and CNRS

### References

- Beatty, J. (1980). Computer Science 688. University of Waterloo, Ontario: Unpublished.
- Beshore, E. (2010, June 02). Access to the CatalinaSky Survey Catalogue (Personal email).
- Bland, P. A., Spurný, P., Towner, M. C., Bevan, A. W., Singleton, A. T., Chesley, S. R., et al. (2009). A Eucrite Delivered from an Aten-type Orbit: The Last Link in the Chain from 4 Vesta to Earth. *40th Lunar and Planetary Science Conference, (Lunar and Planetary Science XL), held March 23-27, 2009 in The Woodlands, Texas, id.1664* .
- Bottke, W. F., Morbidelli, A., Jedicke, R., Petit, J.-M., Levison, H. F., Michel, P., et al. (2002a). Debiased Orbital and Absolute Magnitude Distribution of the Near-Earth Objects. *Icarus* , 156 (2), 399-433.
- Bowell, E., Hapke, B., Domingue, D., Lumme, K., Peltoniemi, J., & Harris, A. W. (1989). Application of photometric models to asteroids. *Asteroids II; Proceedings of the Conference, Tucson, AZ, Mar. 8-11, 1988 (A90-27001 10-91)* , 524-556.
- Brown, P., Spalding, R. E., ReVelle, D. O., Tagliaferri, E., & Worden, S. P. (2002). The flux of small near-Earth objects colliding with the Earth. *Nature* , 420, 294-296.
- Ceplecha, Z. (1987). Geometric, dynamic, orbital and photometric data on meteoroids from photographic fireball networks. *Astronomical Institutes of Czechoslovakia, Bulletin* , 38 (July 1987), 222-234.
- CFHT. (2009, 11 12). *Canada-France-Hawaii Telescope Legacy Survey*. Retrieved 11 14, 2009, from Canada-France-Hawaii Telescope: <http://www.cfht.hawaii.edu/Science/CFHTLS/>
- Gilbert, A. M., & Wiegert, P. A. (2009, June). Searching for main-belt comets using the Canada-France-Hawaii Telescope Legacy Survey. *Icarus* , 201 (2), pp. 714-718.

- Hildebrand, A. R., Milley, E. P., Brown, P. G., McCausland, P. J., Edwards, W., Beech, M., et al. (2009). Characteristics of a Bright Fireball and Meteorite Fall at Buzzard Coulee, Saskatchewan, Canada, November 20, 2008. *40th Lunar and Planetary Science Conference, (Lunar and Planetary Science XL), held March 23-27, 2009 in The Woodlands, Texas, id.2505* .
- Jedicke, R. (2010, May 27). Access to the PanSTARRS Image Catalogue (Private conversation). Breckenridge, Colorado.
- Jenniskens, P., Shaddad, M. H., Numan, D., Elsir, S., Kudoda, A. M., Zolensky, M. E., et al. (2009). The impact and recovery of asteroid 2008 TC3. *Nature* , 458 (7237), 485-488.
- McCausland, P. J., Brown, P. G., Hildebrand, A. R., Flemming, R. L., Barker, I., Moser, D. E., et al. (2010). Fall of the Grimsby H5 Chondrite. *41st Lunar and Planetary Science Conference, held March 1-5, 2010 in The Woodlands, Texas* , p. 2716.
- McMillan, R. (2010, June 01). The Spacewatch image catalogue textual log (Personal email).
- Meeus, J. (1991). *Astronomical Algorithms*. Richmond, Virginia: Willman-Bell, Inc.
- Morbidelli, A., Jedicke, R., Bottke, W. F., Michel, P., & Tedesco, E. F. (2002a). From Magnitudes to Diameters: The Albedo Distribution of Near Earth Objects and the Earth Collision Hazard. *Icarus* , 158 (2), 329-342.
- Spurný, P. (2009, February 27). *State vector for the Bunburra Rockhole meteor (Personal email)* .
- Spurný, P. (1997). Exceptional fireballs photographed in central Europe during the period 1993-1996. *Planetary and Space Science* , 45, 541-555.
- Spurný, P. (2010, May 13). Recent European Network event tables (Personal email).
- Wiegert, P., Balam, D., Moss, A., Veillet, C., Connors, M., & Shelton, I. (2007). Evidence for a Color Dependence in the Size Distribution of Main-Belt Asteroids. *The Astronomical Journal* , 133 (4), 1609-1614.